Article

Nanofibrous Dressing with Nanocomposite Monoporous Microspheres for Chemodynamic Antibacterial Therapy and Wound Healing

Bingjie Xu, Guoqiang Cai, Yujie Gao, Mingchao Chen, Chenlu Xu, Chenglong Wang, Dan Yu, Dongming Qi,* Renhong Li,* and Jindan Wu*

Cite This: ACS Omega 2023, 8, 38481−38493

Read Online

ACCESS | Metrics & More | Article Recommendations | Supporting Information

ABSTRACT: The excessive use of antibiotics and consequent bacterial resistance have emerged as crucial public safety challenges for humanity. As a promising antibacterial treatment, using reactive oxygen species (ROS) can effectively address this problem and has the advantages of being highly efficient and having low toxicity. Herein, electrospinning and electrospraying were employed to fabricate magnesium oxide (MgO)-based nanoparticle composited polycaprolactone (PCL) nanofibrous dressings for the chemodynamic treatment of bacteria-infected wounds. By utilizing electrospraying, erythrocyte-like monoporous PCL microspheres incorporating silver (Ag)- and copper (Cu)-doped MgO nanoparticles were generated, and the unique microsphere-filament structure enabled efficient anchoring on nanofibers. The composite dressings produced high levels of ROS, as confirmed by the 2,7-dichloriflurescin fluorescent probe. The sustained generation of ROS resulted in efficient glutathione oxidation and a remarkable bacterial killing rate of approximately 99% against Staphylococcus aureus (S. aureus). These dressings were found to be effective at treating externally infected wounds. The unique properties of these composite nanofibrous dressings suggest great potential for their use in the medical treatment of bacteria-infected injuries.
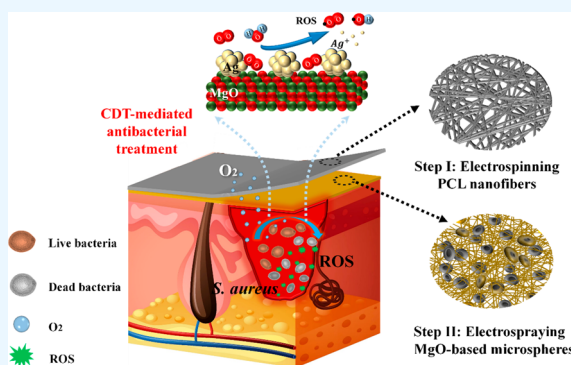
1. INTRODUCTION

Wound infection often occurs in the clinic and can lead to severe complications, including sepsis, septic shock, and even death.[1] Once a skin wound occurs, timely measures must be taken to prevent bacteria from invading the human body and causing infections, which may exacerbate pain and discomfort for the patient and significantly affect their quality of life.[2] Therefore, prompt treatment for bacterial infections in wound healing is crucial. Antibiotics have played a vital role in preventing infections from wounds for decades. However, they are gradually losing effectiveness due to overuse or misuse, known as antibiotic resistance.[3,4] Hence, researchers are developing new antibiotics[5−7] as well as exploring new treatments[8−10] to combat this challenge.

In recent years, minimally invasive therapy based on reactive oxygen species (ROS) has drawn extensive attention,[11,12] including photodynamic therapy (PDT),[13,14] sonodynamic therapy (SDT),[15] and chemodynamic therapy (CDT).[16] These therapies generate ROS to destroy biomolecules such as lipids, proteins, and DNA, thus inducing apoptosis of bacteria and achieving therapeutic effects.[17−19] This approach has shown promising results in combating drug-resistant bacteria,[20,21] providing a potential solution to the issue of antibiotic resistance. As reported by the literature, MgO, as a functional

inorganic material with CDT capability, has unique advantages in generating ROS without external stimulation and an H_2O_2 environment.[22,23] MgO can catalyze dissolved oxygen in water to generate superoxide anion radicals ($O_2^{\bullet-}$) and $^{\bullet}OH$.[24−26] For silver (Ag)- and copper (Cu)-doped MgO nanoparticles (MgO/Ag and MgO/Cu NPs), the catalytic ROS generation activity was improved by accelerating the transfer of electrons to adjacent oxygen vacancies.[27] However, few studies have compared the antibacterial performance of MgO/Ag and MgO/Cu nanoparticles as Ag and Cu may have different intrinsic toxicity and effects on ROS generation.

The direct application of nanosized powders on infected wounds can lead to uncontrolled diffusion, causing severe biotoxicity or complications.[28] To address this issue, combining inorganic NPs with polymer matrixes is a widely adopted strategy. Among various polymer matrixes, nanofibers
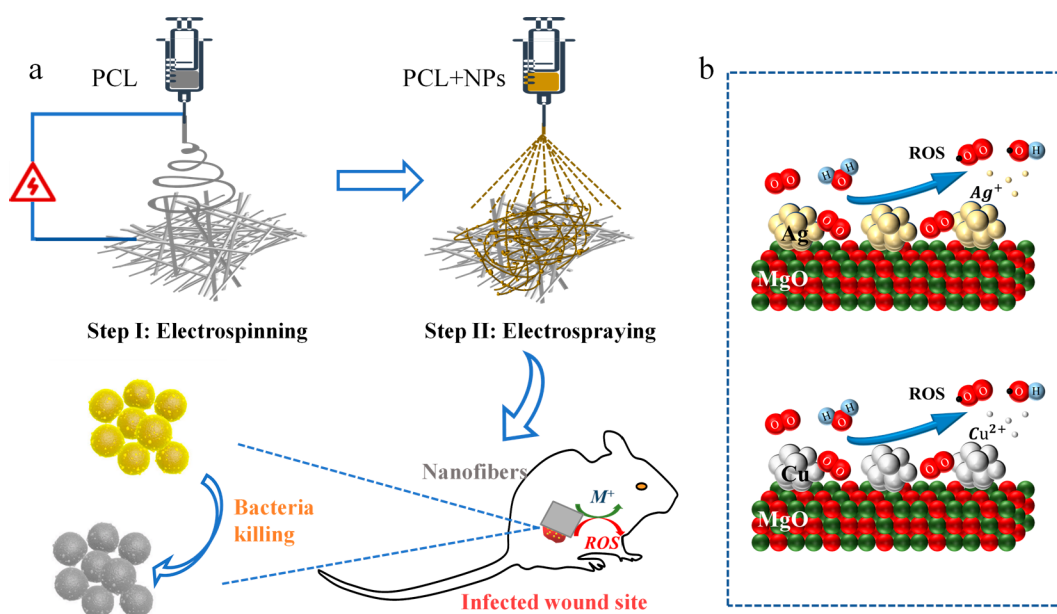
Figure 1. (a) Schematic illustration of the preparation of MgO/Ag-PCL or MgO/Cu-PCL nanofibers and their applications in wound healing. (b) Schematic diagrams of ROS produced by MgO/Ag and MgO/Cu NPs.

received significant attention due to their extracellular matrix-like structural and physical characteristics, high specific surface area, high porosity, and excellent mechanical and biological properties.[29] Blend electrospinning is the most direct way to obtain NP−composite nanofibers,[30] which can be used as dressings for wound healing. However, reduced activity of NPs has been found due to encapsulation in the fiber matrix. Although other strategies, including coaxial electrospinning techniques,[31] in situ growth approaches,[32] suction filtration,[33] and others, can achieve the surface enrichment of NPs, they face challenges such as complicated devices, harsh preparation processes, and poor stability.

Electrospraying is an electrofluidic atomization process that utilizes a high-voltage electric field to transform low-viscosity Newtonian liquids into minute droplets.[34] By manipulating electrospraying parameters, this technique enables the production of polymer micro/nanospheres with controllable size and different surface morphology in a single step, providing new thoughts for developing loaded nanoparticles or drugs with different functions.[35,36] For example, Ali et al. prepared the complexes with various structural morphologies exhibiting different drug release behaviors by optimizing the process parameters.[37] Thus, electrospraying combined with the electrospinning process is considered as a convenient and effective method for preparing nanoparticle composite nanofiber dressing.

In this study, we developed MgO-based monoporous composite microsphere/polycaprolactone (PCL) nanofibrous dressings with chemodynamic antibacterial effects for the treatment of infected wounds. The composite nanofibrous dressing was obtained through electrospinning and electrospraying techniques. Specifically, the PCL nanofibrous membrane, serving as the substrate, was prepared by electrospinning, while the monoporous composite microspheres of MgO/Ag or MgO/Cu NPs, accompanied by PCL ultrafine fibers, were prepared by electrospraying (Figure 1a). It was anticipated that the monoporous composite microspheres would enhance the contact between the loaded MgO-

based catalyst and the substrate (water and oxygen), thereby enhancing the reaction activity. We investigated the chemodynamic characteristics of the composite dressings and evaluated their antibacterial performance in vitro and in vivo. Additionally, we assessed the effects of the composite dressings on wound healing. Overall, the composite nanofibrous dressing, which has the ability to generate ROS, represents a promising approach for the effective management of infected wounds.

2. EXPERIMENTAL SECTION

2.1. Materials and Chemicals. PCL (M_w = 80000) and 2,7-dichlorodihydrofluorescein diacetate (DCFH-DA) assays were purchased from Sigma-Aldrich Company (USA). 2,2,2-Trifluoroethanol (TFEA, 99.5%), reduced glutathione (GSH), and 5,5′-dithiobis(2-nitrobenzoic acid) (DTNB) were purchased from Aladdin Biochemical Technology Co., Ltd. (Shanghai). *Escherichia coli* (*E. coli*, ATCC 8099) and *Staphylococcus aureus* (*S. aureus*, ATCC 6538) were purchased from Shanghai Luwei Technology Co., Ltd., and DMEM, fetal bovine serum (FBS), penicillin/streptomycin (double antibody), and cell countering kit-8 (CCK-8) reagents were purchased from Jinbai Technology Co., Ltd. (Hangzhou).

2.2. Preparation of Composite NPs. MgO/Ag and MgO/Cu composite NPs were prepared by using the colloidal deposition method.[38,39] To synthesize MgO NPs, a mixture of 6.2 mL of magnesium methoxide and 100 mL of methanol was sonicated for 10 min. The sonicated mixture was then hydrolyzed with 200 mL of deionized water at 80 °C for 6 h. The resulting product was washed multiple times with ethanol and deionized water, collected through centrifugation, and dried overnight at 80 °C. The dried product was further calcined at 450 °C in air for 5 h.

To synthesize Ag or Cu NPs, different procedures were followed. For Ag NPs, 110 mg of AgCF₃COO was dissolved in a mixture of 250 μL of dodecanethiol and 50 mL of benzene under a flow of H₂/Ar (5 v/v%) gas. To this solution, 435 mg of borane−*tert*-butylamine complex (BTBC) was added. The

mixture was heated with stirring at 55 °C for 2 h and then cooled to room temperature. Ag NPs were precipitated by adding 20 mL of ethanol to the reaction mixture, followed by centrifugation, washing with ethanol, and drying under a H_2/Ar flow.

For Cu NPs, 66.6 mg of $Cu(acac)_2$ was dissolved in a mixed solution of 200 μL of dodecanethiol and 40 mL of benzene under a flow of H_2/Ar (5 v/v%) gas. 200 mg of BTBC was then added to the solution. The mixture was heated with stirring at 55 °C for 6 h and cooled to room temperature. Cu NPs were precipitated, washed, and dried using the same procedure as that for the Ag NPs.

Composite NPs were prepared through a colloidal deposition method by loading either Ag NPs or Cu NPs onto MgO NPs. 5 mg of Ag NPs or Cu NPs was dispersed in 25 mL of chloroform. Subsequently, 495 mg of MgO NPs was added to the solution. After being stirred for 30 min, the solid product was collected through centrifugation and dried in N_2. The resulting composite powder was calcined at 450 °C for 5 h in a flow of 5 v/v% H_2/Ar.

2.3. Preparation of MgO/Ag or MgO/Cu Composite Nanofibrous Dressings. The electrospinning solution was prepared as follows: First, PCL (1.0 g) was dissolved in 10 mL of TFEA at 60 °C with magnetic stirring and then stirred at room temperature for another 4 h to obtain a uniform and transparent PCL solution (10%, w/v). The electrospinning of PCL was carried out using electrospinning equipment (YFSP-T, Yunfan Technology Co., Ltd., Tianjin, China). The electrospinning parameters were optimized as follows: the applied voltage was 15 kV; the distance from the syringe tip to the drum collector was 15 cm; the advancing speed of the syringe pump was 1.8 mL/h; and the spinning time was 3 h. During the electrospinning, the temperature and relative humidity were maintained at 28 $\pm$ 2 °C and 60 $\pm$ 5% RH, respectively.

The preparation parameters of monoporous composite microspheres, including polymer concentration, temperature, and humidity of the electrospray, were optimized. First, the concentration of polymer solutions was investigated by dissolving different contents of PCL (0.5%, 1%, 2%, 2.5%, and 3% (w/v)) and dispersing the same content of MgO/Ag NPs (0.4% (w/v)) in TFEA, and then these solutions were electrosprayed under identical spinning conditions. Second, electrospraying was performed by changing the temperature (23 $\pm$ 2, 28 $\pm$ 2, and 33 $\pm$ 2 °C) and humidity (30 $\pm$ 5%, 60 $\pm$ 5%, and 75 $\pm$ 5% RH) during the spinning process under the same spinning solution (2% (w/v) PCL and 0.4% (w/v) MgO/Ag NPs) and other spinning conditions. The optimized electrospraying procedure was obtained as the above. Specifically, the electrospraying solution was prepared by dissolving PCL in TFEA (2.5% (w/v)). Next, MgO/Ag or MgO/Cu NPs was dispersed in the above PCL solution to obtain a uniform NP suspension with a content of 0.4% (w/v). Before being electrosprayed, the suspension was sonicated for 20 min (KQ-200 KDE, Kunshan Ultrasonic Instrument Co., Ltd.). The mixture was placed in a 5 mL plastic syringe with a 22 gauge stainless steel needle and pumped by a propeller pump. The electrospraying parameters were as follows: the applied voltage was 12 kV; the receiving distance was 13 cm; the flow rate was 1.8 mL/h; the temperature and humidity were maintained at 33 $\pm$ 2 °C and 60 $\pm$ 5% RH, respectively; and electrospraying was carried out for 3 h. The prepared nanocomposite dressings containing MgO/Ag and MgO/Cu

were labeled as MgO/Ag-PCL and MgO/Cu-PCL, respectively.

2.4. Characterization. The morphology and element distribution of the nanocomposite dressings were examined by scanning electron microscopy (SEM, JSM-5610 LV, Nippon Electronics Co., Ltd.) equipped with an energy dispersive spectrometer (EDS). To determine the diameter of the nanofibers and the size of the microspheres, a total of 80 nanofibers and 30 microspheres were randomly selected from SEM images and analyzed using ImageJ software. The crystal structures of MgO/Ag and MgO/Cu were characterized by X-ray diffraction (XRD, A8 Advance, Bruker AXS). The content of metal elements in the nanofibers was tested by an inductively coupled plasma mass spectrometer (ICP-MS, Optima 8300DV/CPMS, NexION 300X, PerkinElmer, USA). A video-based contact angle measuring device (FM40MK2, Kruss, Germany) was used to measure the water contact angles (WCAs) of the prepared dressings. The mechanical tensile properties of the dressings were tested by using a universal material testing machine (Instron 3367, ITW Group Yingstrong Company). Fluorescence images of nanofibers incubated with DCFH were observed and recorded by using a confocal laser scanning microscope (CLSM, C2, Nikon Instrument Co., Ltd., Japan).

2.5. Determination of Released Metal Ions. MgO/Ag-PCL and MgO/Cu-PCL with a size of 2 × 2 cm^2 were immersed in 5 mL of PBS solution, followed by shaking in an oscillating incubator (TQZ-312, Shanghai Jinghong Experimental Equipment Co., Ltd.) at 37 °C and 150 rpm for 24 h. The contents of Ag and Cu in the solution were determined by ICP-MS.

2.6. Characterization of the Chemodynamic Properties. The chemodynamic property, i.e., the capability of ROS generation, was characterized by using 2,7-dichlorodihydrofluorescein (DCFH) as a chemical probe. DCFH (200 μM) was obtained by mixing the DCFH-DA solution (DMSO, 1 mM) with the sodium hydroxide solution (NaOH, 10 mM) at a volume ratio of 1:4 and then stirring continuously for 30 min in the dark. Before use, it was diluted to 10 μM with a PBS solution (pH = 7.4). 100 μg/mL MgO/Ag or MgO/Cu aqueous suspension was mixed with DCFH solution at a volume ratio of 1:9 and reacted at room temperature for 1 h. The fluorescence spectra of the mixture were collected every 10 min during the test using a fluorescence spectrophotometer (F-46001, Hitachi, Japan). Similarly, 2 × 2 cm^2 composite microspheres (nonporous microspheres and monoporous microspheres electrosprayed on tin foil) or composite fibrous dressings (MgO/Ag-PCL or MgO/Cu-PCL) was immersed in 5 mL of DCFH solution and reacted for a certain time at room temperature. The fluorescence spectra were also recorded at fixed time intervals.

2.7. Detection of ROS Type. The type of ROS generated by the two nanocomposite dressings was tested by electron spin resonance (ESR, A300-10/12, Bruker, Germany). First, 1 × 1 cm^2 MgO/Ag-PCL or MgO/Cu-PCL was immersed in 1 mL of PBS solution (pH 7.4) for 10 min, and then 100 μL of solution was removed, followed by the addition of 100 μL of DMPO solution (100 mM). Finally, the ESR spectrum of the mixed solution was recorded. The test parameters were as follows: modulation frequency was 100.00 kHz; modulation amplitude was 1.00 G; center field was 3510.00 G; scan width was 100.00 g; time constant was 10.24 ms; conversion was 40.000 ms; scanning time was 30.72 s; receiver gain was 1.02 ×

10^3; microwave power was 19.24 mW; and microwave frequency was 9.8517 GHz.

2.8. In Vitro Antibacterial Study. The antibacterial study was carried out according to standard procedures.[40,41] Two representative bacteria, *S. aureus* and *E. coli*, were used to evaluate the antibacterial activity of the composite nanofibers. In detail, *S. aureus* and *E. coli* were inoculated separately in sterile liquid medium and shaken overnight at 37 °C with a speed of 150 rpm until the logarithmic growth phase was reached. Then, three fibrous dressings (MgO/Ag-PCL, MgO/Cu-PCL, and PCL) with a size of 2×2 cm^2 were immersed separately into 5 mL of bacterial suspensions (approximately 1 $\times 10^7$ CFU/mL) and incubated for 4 h (37 °C, 150 rpm). Subsequently, the bacterial suspensions were diluted to different concentration gradients, and 100 μL of the diluted bacterial suspension was inoculated on LB agar plates and cultured at 37 °C for 24 h (water-jacket thermostatic incubator, GHP-9050, Shanghai Yiheng Scientific Instruments Co., Ltd.). Photographs of plates were taken, and the bacterial colonies were counted. The antibacterial activity of the different samples can be calculated as follows:

$$\text{antibacterial activity (\%)} = \frac{N_{\text{control}} - N_{\text{sample}}}{N_{\text{control}}} \times 100$$

where N_{control} and N_{sample} are the number of colonies of bacteria treated with PCL and nanocomposite dressings, respectively.

2.9. Observation of Bacterial Morphology. According to the standard antibacterial test procedures, the dressings cocultured with a bacterial suspension were gently removed after ultrasonic treatment for 3 min. The remaining bacteria were gathered by centrifugation, which was further washed 3 times with 1 mL of PBS solution (pH = 7.4) (10000 rpm, 5 min) (H1850, Xiangyi Laboratory Instrument Development Co., Ltd., Hunan) and then successively immersed in 2.5% glutaraldehyde buffer solution at 4 °C for 2 h. After that, the bacteria were dehydrated with 10%, 30%, 50%, 70%, 80%, 90%, and 100% ethanol for 15 min. Finally, the prepared bacterial suspension was dripped onto cleaned silicon wafers, dried naturally, and observed by SEM.

2.10. Antioxidation of GSH. DTNB stock solution (0.1 M) was prepared with a buffer solution of Na_2HPO_4 (0.05 M, pH = 8.7) and diluted 100 times with Tris−HCl buffer (0.05 M, pH = 8.0) to obtain the DTNB analysis solution, which was kept in the dark before use. Three dressings (PCL, MgO/Ag-PCL, and MgO/Cu-PCL) were put into 5 mL of GSH/Na_2HPO_4 buffer solution (0.5 mM) and incubated at 37 °C for 4 h. Subsequently, the dressings were removed, and 5 mL of DTNB analytical solution was added. DTNB was reduced to yellow 5-thio-2-nitrobenzene (TNB) by the residual GSH in the solution. The concentration of TNB was detected by an ultraviolet−visible spectrophotometer (Lambda 35, Perkin-nElmer, USA) at 412 nm. The loss of GSH from the solution can be calculated by using the following equation

$$\text{GSH loss (\%)} = \frac{A_{\text{control}} - A_{\text{sample}}}{A_{\text{control}}} \times 100$$

where A_{control} and A_{sample} are the absorbances of the solution treated with PCL and nanocomposite dressings, respectively.

2.11. Cytotoxicity Test. The cytotoxicity of the nanocomposite dressings was evaluated by using the standard CCK-8 assay. DMEM containing 10% FBS and 100 U/mL double-antibody were adopted for the culture of NTH/3T3 mouse fibroblasts. The cells were inoculated in a 96-well plate (25000 cells/well) and cultured in a CO$_2$ incubator (MCO-18AIC-(UV), Sanyo Electric Co., Ltd., Osaka, Japan) (37 °C, 5% CO$_2$) for 24 h. PCL, MgO/Ag-PCL, and MgO/Cu-PCL with a diameter of 6 mm were gently added to each well (5 parallel experiments for each sample). After incubation for another 24 h, the dressings were removed and 10 μL of CCK-8 standard reagent solution was added to each well. After 2 h of incubation, the optical density (OD) at 450 nm was measured using a microplate reader (Multiskan FC, Thermo Fisher Scientific), and the cell viability was determined by the following equation

$$\text{viability rate (\%)} = \frac{\text{OD}_{\text{sample}} - \text{OD}_{\text{blank}}}{\text{OD}_{\text{control}} - \text{OD}_{\text{blank}}} \times 100$$

where OD_{blank} represents the OD value of the DMEM and CCK-8 reagent. $\text{OD}_{\text{control}}$ represents the OD value of the untreated cells. $\text{OD}_{\text{sample}}$ represents the OD value of cells treated with PCL and nanocomposite dressings.

2.12. Animal Wound Healing Experiment. The study was approved by the Experimental Animal Ethics Committee, Zhejiang Sci-Tech University (reference no. 20210626-01) and followed the Guide for the Care and Use of Laboratory Animals. Female ICR mice (6−8 weeks) were used to evaluate the effect of nanofibrous dressings on in vivo wound healing. These mice were purchased from the Zhejiang Laboratory Animal Center and acclimatized for 6−7 days before any treatments. First, these mice were anesthetized, and then 100 μL of *S. aureus* (1×10^8 CFU/mL) was injected subcutaneously into the back of each mouse. 24 h later, a full-thickness cutaneous injured wound of 8 mm diameter was established on the infected site of each mouse. Then, the mice were randomly divided into four groups (n = 6 in each group): gauze group (control group), PCL, MgO/Ag-PCL, and MgO/Cu-PCL. Different dressings with a size of 8 mm covered the wound site. On day 1 and 2, bacteria from the wounds were collected using sterile cotton swabs and transferred into 3 mL of sterilized PBS solution. The bacterial suspension was evenly spread on LB agar for incubation and counting. In addition, the dressings were changed, and the wounds were observed and photographed on days 0, 1, 2, 4, 6, 8, and 11. The wound areas at different time points were measured, and the ratio (%) of the relative wound area was calculated as follows

$$\text{relative wound area (\%)} = \frac{S_1}{S_0} \times 100$$

where S_1 represents the current wound area and S_0 represents the initial wound area.

2.13. Statistical Analysis. All data are expressed as the mean ± standard deviation (SD). Statistical comparisons were shown by one-way analysis of variance (ANOVA). $P < 0.05$ was deemed significant ($*P < 0.05$, $**P < 0.01$), and $P > 0.05$ was not statistically significant (ns).

3. RESULTS AND DISCUSSION

3.1. Preparation and Characterization of MgO-based NPs. According to the report, doping Ag and Cu into MgO introduces oxygen vacancy site (OVS) defects, promotes the conversion of excitons to carriers, and accelerates the surface reduction half-reaction for carrier separation (ROS generation).[42] Furthermore, they create new active sites that act synergistically with OVS to accelerate ROS generation.[43,44] As
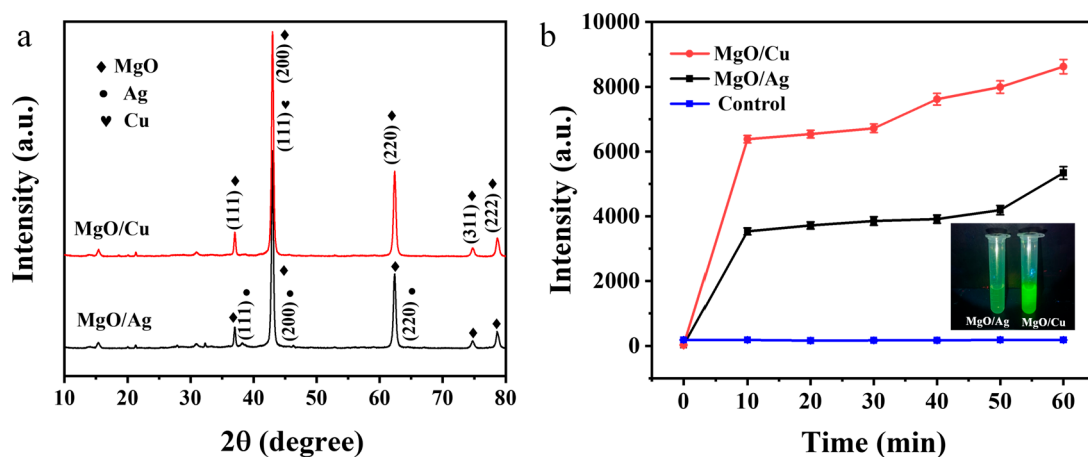
Figure 2. (a) XRD spectrogram of MgO/Ag and MgO/Cu NPs. (b) Variation in the DCFH fluorescence intensity of MgO/Ag or MgO/Cu NPs with time detected at 522 nm by a fluorescence spectrophotometer; the inset shows a fluorescent photograph of solutions after the reaction of the corresponding nanoparticles with DCFH.
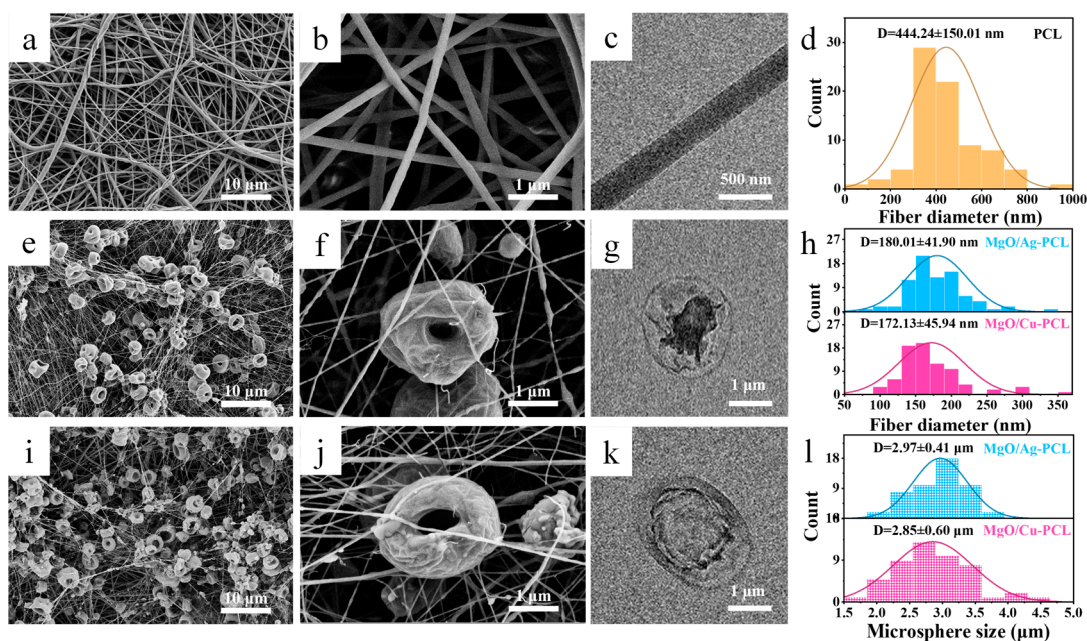

Figure 3. SEM images at low and high magnification and TEM images of (a−c) PCL, (e−g) MgO/Ag-PCL, and (i−k) MgO/Cu-PCL. Diameter distributions of (d, h) ultrafine fibers and (l) microspheres.

shown in Figure 1b, MgO/Ag or MgO/Cu NPs could catalyze the production of ROS from adsorbed oxygen. Hence, these two composite particles were utilized as antibacterial components in composite nanofibrous dressing.

The two MgO-based NPs doped with Ag or Cu were easily prepared by the colloidal deposition method, exhibiting a two-dimensional sheetlike structure (Figure S1a,c). EDS measurements demonstrated that the atomic content of Ag or Cu loaded on the surface of MgO accounted for approximately 1% of the total amount (Figures S1b,d), confirming the successful doping of Ag or Cu to MgO composites. Meanwhile, the XRD pattern provided structural information about the composite NPs (Figure 2a). All diffraction peaks of MgO composite NPs matched well with face-centered cubic phase MgO (Joint Committee on Powder Diffraction Standards (JCPDS) 77-2364). The crystal structure of Ag or Cu was not evident in the spectra due to their low concentration, and the peaks overlapped with the characteristic diffraction peaks of MgO.

To assess the ROS generation performance of the composite NPs upon exposure to water, DCFH was adopted as a chemical fluorescence probe to detect ROS levels. DCFH is nonemissive but can be converted into fluorescent dichloro-fluorescein (DCF) after oxidation (Figure 2b). DCF emits fluorescence at approximately 522 nm, and the intensity correlates with ROS production. In both the MgO/Cu and MgO/Ag groups, a substantial increase in the fluorescence intensity was observed in the first 10 min (Figures 2b and S2). It was indicated that the composite NPs were in direct and complete contact with the aqueous solution, catalyzing the adsorbed oxygen or oxygen in the water to generate ROS rapidly,[45,46] which further reacted with DCFH to produce DCF. As time progressed, the fluorescence intensity increased slowly due to the depletion of oxygen in the water. In addition, the fluorescence intensity of the MgO/Cu group was higher than that of the MgO/Ag group in the presence of DCFH, which could be attributed to the fact that Cu has a stronger
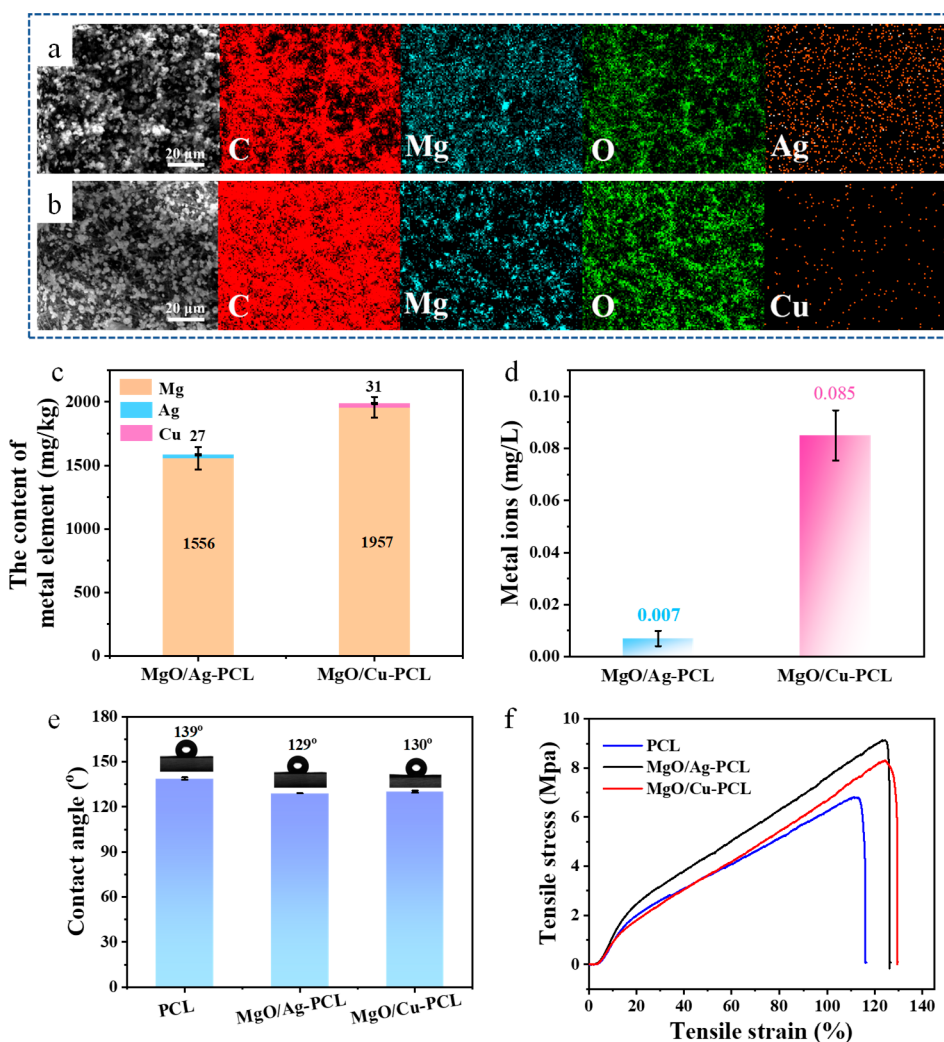
Figure 4. Elemental mappings of (a) MgO/Ag-PCL and (b) MgO/Cu-PCL detected by EDS. The contents of Mg, Ag, and Cu elements in (c) the nanocomposite dressing and (d) its leaching solution were determined by ICP−MS. (e) Water contact angles and (f) stress−strain curves of the nanocomposite dressings.

capability in preventing recombination of electron−hole pairs.[47,48]

3.2. Preparation and Characterization of MgO-Based Composite Nanofibrous Dressings.

MgO-based NP-composited nanofibrous dressings were prepared by combining electrospinning and electrospraying technology. As shown in Figure 3a−d, the PCL layer presented a typical nanofiber structure with mean fiber diameter of 444.24 ± 150.01 nm. The structure of electrosprayed monoporous composite microspheres was easily regulated by polymer concentration as well as temperature and humidity. First, morphological structures were investigated with different concentrations of PCL solution spinning (Figure S3). In the same experimental conditions, 0.5% and 1% (w/v) PCL blends could not form uniform composite microspheres, as the particles could not be completely encapsulated by the small amount of polymer. On the other hand, 2% and 2.5% (w/v) PCL mixtures led to microsphere structures with a moderate collapse into pores. It was assumed that during the electrospraying process, the low-concentration PCL formed a shell on the air−liquid interface of the droplets produced through electrospray dispersion due to the rapid evaporation of the solvent. Nevertheless, the thin polymer shell was unable to resist the compressive force

generated by further solvent evaporation inside the droplets, leading to the collapse of microspheres into structures similar to red blood cells.[49] Upon further increasing the PCL content to 3% (w/v), the formation of fibers became more prevalent while the number of microspheres was reduced. To ensure a more reliable attachment of the microspheres to the PCL nanofibers, a 2.5% (w/v) polymer solution capable of forming a certain number of ultrafine fibers was selected. Additionally, our results indicate that the formation of microspheres with pores occurred exclusively under specific temperature and humidity conditions. Specifically, we observed that the formation occurred at a temperature range of 33 ± 2 °C, coupled with either a humidity level of 60 ± 5% RH or 75 ± 5% RH (Figure S4). Interestingly, no such formation was observed under any other temperature and humidity settings. The chemodynamic properties of monoporous composite microspheres and microspheres without pores were compared. As shown in Figure S5, it was found that the presence of pores indeed increased the rate of ROS production.

As shown in Figure 3e−l, the electrospray layer prepared under the conditions mentioned above consisted of ultrafine fibers, with an average diameter of 180.01 ± 41.9 nm for MgO/Ag-PCL or 172.13 ± 445.94 nm for MgO/Cu-PCL as
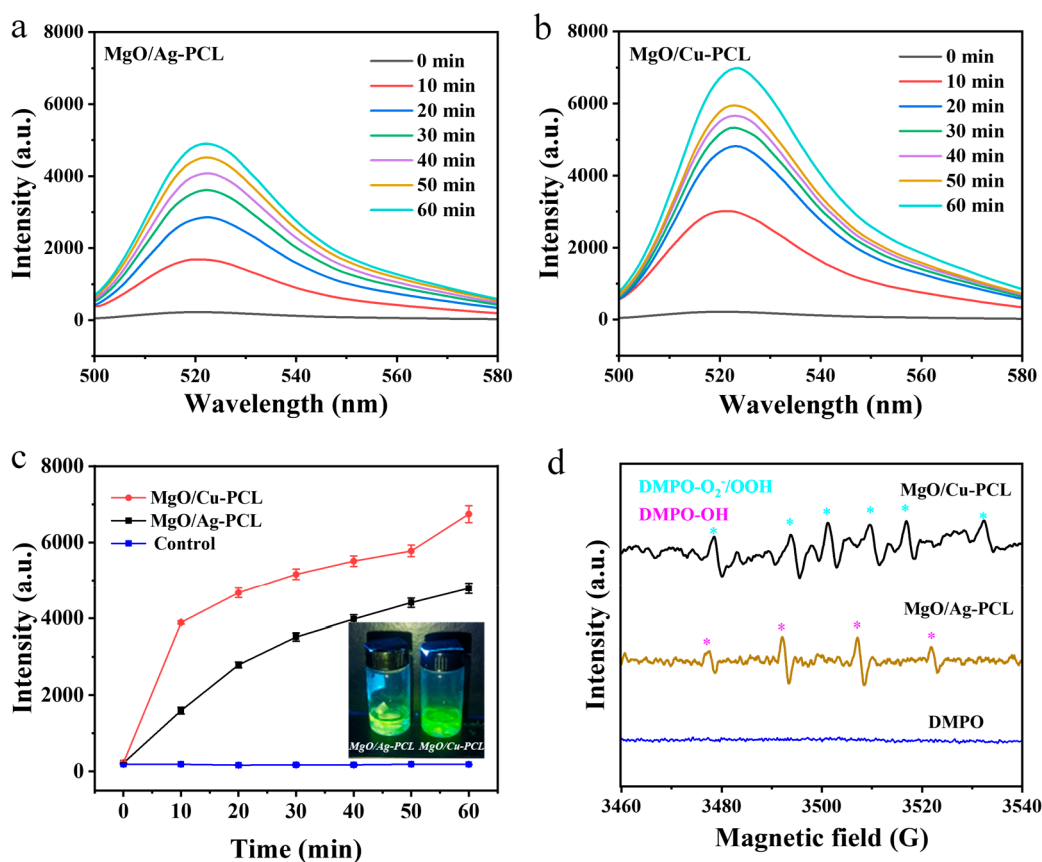
Figure 5. (a, b) Fluorescence emission spectra and (c) fluorescence intensity of the reaction solution of MgO/Ag-PCL and MgO/Cu-PCL with DCFH at different times. The insets are photographs of the reaction solutions. (d) ESR spectra of radicals captured by DMPO in PBS solutions containing MgO/Ag-PCL or MgO/Cu-PCL.

well as microspheres with an average size of 2.97 ± 0.41 μm for MgO/Ag-PCL or 2.97 ± 0.6 μm for MgO/Cu-PCL. These microspheres exhibited a flat disk-shaped red blood cell structure with a central depression forming a pore. TEM images revealed that the particles were enclosed in microspheres with a thin polymer shell layer.

The distribution and content of inorganic NPs in the nanocomposite dressings were further investigated by EDS and ICP. MgO/Ag and MgO/Cu NPs were found to be well-dispersed on the nanofiber surface (Figure 4a,b). Based on ICP results, the mass of Mg accounted for approximately 0.16% and 0.20% of the MgO/Ag-PCL and MgO/Cu-PCL, respectively, while Ag and Cu accounted for only 0.0027% and 0.0031% of their corresponding nanofibers (Figure 4c). These findings confirmed the successful loading of MgO/Ag and MgO/Cu NPs onto nanofibrous dressings. Furthermore, it was found that the leaching solution from the nanofibers contained only trace amounts of approximately 0.007 mg/L Ag and 0.085 mg/L Cu (Figure 4d). The content of Cu was higher than that of Ag in the solution, resulting from the stronger metallic activity of Cu compared to Ag.[50]

The surface wettability and mechanical properties of wound dressings are crucial to their therapeutic effect. To this end, the wetting behaviors of the water droplets on the nanofibers were investigated. As shown in Figure 4e, PCL, MgO/Ag-PCL, and MgO/Cu-PCL were hydrophobic, with water contact angles (WCAs) of 139°, 129°, and 130°, respectively. The WCA of the nanocomposite dressing decreased by approximately 10°, possibly due to the hydrophilic nature of the NPs.[51] Overall,

the hydrophobic wound dressing developed here was expected to have the advantage of not adhering to the wound.[52] In addition, the mechanical properties of the nanofibrous dressings were evaluated. As shown in Figure 4f, the fracture stress of the pure PCL nanofibrous dressing was 6.79 MPa, whereas those of MgO/Ag-PCL and MgO/Cu-PCL increased by 2.34 and 1.52 MPa, respectively. It was demonstrated that the string-bead structured layer enhanced the mechanical properties of the nanofibrous dressing.

Subsequently, the CDT activity of the nanocomposite dressings was investigated. Similarly, a DCFH chemical probe was used to study the process of spontaneous ROS generation. The nanofibers were reacted with the DCFH solution for 10 min and then exposed to a 488 nm laser with the emitted light in the range 490−530 nm. The results were observed with CLSM and photographed. PCL showed no fluorescence after reacting with DCFH, indicating that PCL could not produce ROS (Figure S6). However, substances with clear and green fluorescence were found on the nanocomposite dressings after reacting with DCFH, indicating that ROS was generated and released from the dressings. These results suggested that MgO/Ag and MgO/Cu composite NPs are the primary causes of ROS production in these nanocomposite dressings.

Additionally, the fluorescence intensities of DCF in the solution at different reaction times were also measured using a fluorescence spectrophotometer (Figure 5a, b). The green and fluorescent substance DCF was detected in the solution, and the fluorescence intensity at λ = 522 nm increased with time
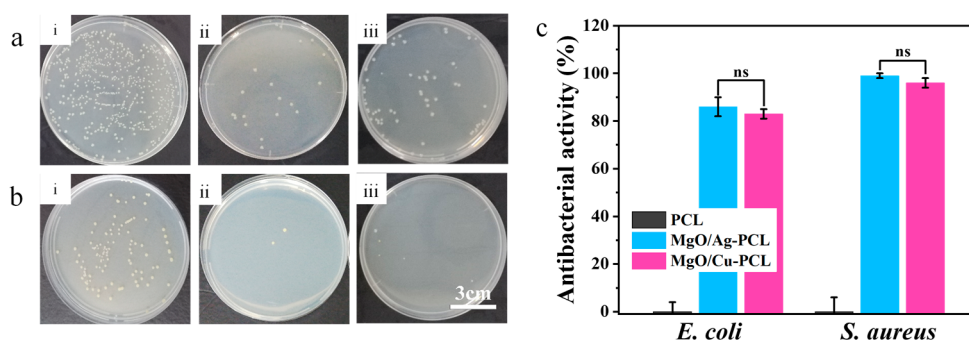
Figure 6. (a, b) Photographs of *E. coli* and *S. aureus* colonies grown on agar plates after coculture with different nanofibrous dressings (i: PCL; ii: MgO/Ag-PCL; iii: MgO/Cu-PCL). (c) Histogram showing the killing rate of bacteria. Significant difference: $P > 0.05$ (ns).
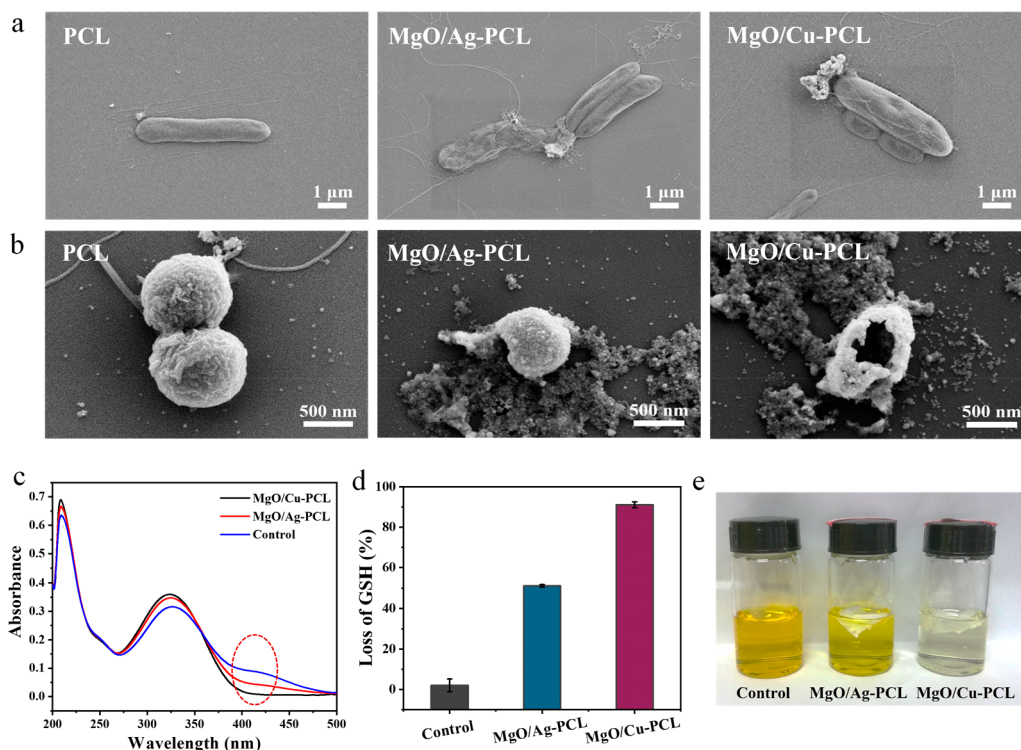

Figure 7. (a, b) SEM images of bacteria after contact with different nanofibrous dressings (i: PCL; ii: MgO/Ag-PCL; iii: MgO/Cu-PCL). (c) UV absorption curves of nanofibrous dressings after incubation with GSH followed by reaction with DTNB. (d) Histogram of GSH loss of different nanofibrous dressings. (e) Corresponding photo of the reaction solution.

(Figure 5c). The intensity of the MgO/Cu-PCL group was stronger than that of the MgO/Ag-PCL group, consistent with the results of the corresponding NPs. The MgO-based NPs were partially encapsulated in PCL microspheres and gradually contacted oxygen in the water until oxygen in the water was totally consumed. Thus, a gradual production of ROS and a slow increase in fluorescence intensity were observed, whereas the MgO-based NPs exhibited an abrupt increase in ROS levels initially and slowed after 10 min. It was revealed that ROS could be continuously released through the nano-composite nanofibers, which prolongs the antibacterial effect.

The type of ROS generated by the nanocomposite dressings was determined. The samples were incubated in PBS (pH 7.4) for 10 min, and the generated ROS were rapidly captured using the trapping agent DMPO. As shown in the ESR/EPR spectrum (Figure 5d), a blue asterisk-marked signal and a rosy asterisk-marked signal were found, which can be attributed to DMPO adducts with $O_2^{\bullet-}/HOO^-$ and $^{\bullet}OH$, respec-

tively.[38,53,54] Among them, $O_2^{\bullet-}$ is a single-electron reduction product of the ground state oxygen that can transform into hydroperoxyl radicals (HOO^-) by accepting H^+,[55] and the two are in equilibrium in an aqueous solution. Although only a small amount of $O_2^{\bullet-}$ was converted to HOO^- under simulated physiological conditions at pH 7.4, the oxidation effect of HOO^- is much greater than the oxidation effect of $O_2^{\bullet-}$. On the other hand, $^{\bullet}OH$, a highly reactive three-electron-reduction product of O_2, which can react with almost all cellular components, was obtained after a series of reactions of $O_2^{\bullet-}$. It was found that MgO/Cu-PCL mainly generated $O_2^{\bullet-}$ and HOO^-, while MgO/Ag-PCL generated $^{\bullet}OH$. This difference might be attributed to the different ROS production mechanisms of the composite NPs doped with Ag or Cu.

3.3. In Vitro Antibacterial Activity Test. An in vitro antibacterial test was conducted to evaluate the effectiveness of MgO/Cu-PCL and MgO/Ag-PCL in killing bacteria. *E. coli* and *S. aureus* were used as examples, and the plate count
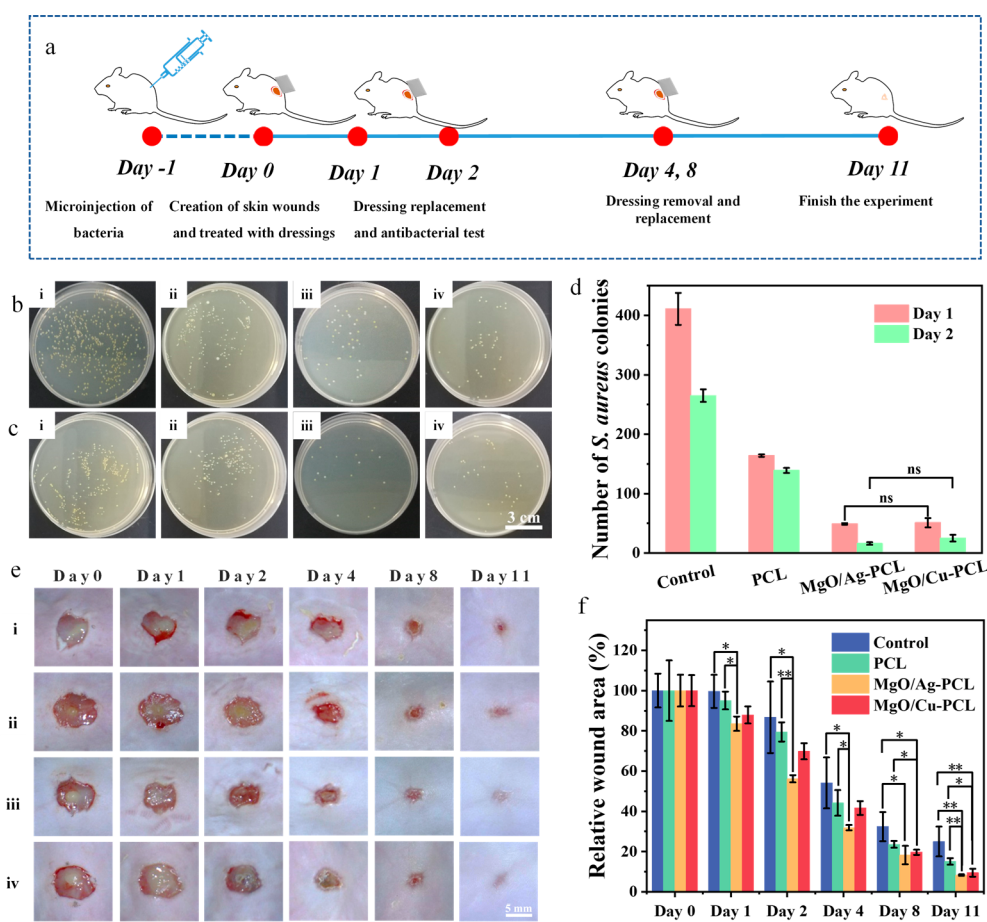
Figure 8. (a) Establishment and treatment process of the full-thickness skin infection model. (b, c) Photographs of colonies grown on agar plates with different nanofiber dressings in the initial stage and (d) the corresponding histogram. (e) Photographs of wounds in different groups of mice at different times during the treatment. (f) Evaluation of wound area changes on the first, second, fourth, eighth, and 11th days after treatment in different groups (i: control; ii: PCL; iii: MgO/Ag-PCL; iv: MgO/Cu-PCL). Significant difference: *$P < 0.05$, **$P < 0.01$, and $P > 0.05$ (ns).

method was employed to demonstrate the antibacterial activity of the composites. PCL did not exhibit any antibacterial activity against either bacteria, while MgO/Cu-PCL and MgO/Ag-PCL achieved antibacterial ratios of $83 \pm 2\%$ and $86 \pm 4\%$ against *E. coli* and $96 \pm 2\%$ and $99 \pm 1\%$ against *S. aureus*, respectively (Figure 6). This result indicated that the ROS generated by the nanocomposite dressings could effectively kill bacteria. In addition, the bactericidal effect of both nanocomposite dressings against Gram-positive *S. aureus* was higher than that against Gram-negative *E. coli*, which might be attributed to the different structures of the two bacteria.[14] Gram-negative bacteria have a bilayer structure with the outer membrane being a dense layer of lipopolysaccharides and lipoproteins, acting as a strong barrier to prevent the penetration of antimicrobial components into the cell wall. However, the cell wall of Gram-positive bacteria mainly consists of an open network of peptidoglycan, teichoic acid, and lipoteichoic acids, making it more susceptible to antibacterial substances. In addition, although no significant difference was found in the antibacterial efficiency between MgO/Ag-PCL and MgO/Cu-PCL, the antibacterial efficiency of the former was slightly higher than that of the latter, which was inconsistent with the CDT activity characterization results. The phenomenon can be explained by the different types of ROS produced by MgO/Ag and MgO/Cu. In the case of MgO/Ag, it primarily generates $^\bullet$OH, while MgO/Cu

predominantly produces $O_2^{\bullet-}/HOO^-$. The stronger oxidation ability of $^\bullet$OH exhibited by MgO/Ag compared to $O_2^{\bullet-}/HOO^-$ in MgO/Cu enables MgO/Ag to more effectively inhibit bacterial growth. Although the total amount of ROS produced with MgO/Ag is slightly lower than that with MgO/Cu, its oxidation ability toward bacteria is stronger, resulting in a slightly higher antibacterial property.

3.4. Antibacterial Mechanism of Nanocomposite Nanofibers. It has been reported that ROS can damage cell membranes by inducing lipid peroxidation and thus enhancing their permeability, which is the main mechanism for intracellular leakage and bacterial death.[56] Hence, the bacterial morphology was further observed. Both *E. coli* and *S. aureus* in the control group possessed smooth surfaces with rod-shaped and spherical structures (Figure 7a,b). However, the bacterial membranes in the experimental group were disrupted, appearing wrinkled, collapsed, and fractured to some extent. In addition, more severe damage was observed in *S. aureus*, which may be caused by its simpler cell wall structure. These results suggested that the nanocomposite dressings effectively produce ROS and destroy the bacterial membrane structure, ultimately leading to bacterial death.

GSH is the most abundant sulfhydryl-containing small molecular peptide and widely exists in all kinds of bacteria, with a concentration of 0.1−10 mM. It participates in the redox reaction in bacterial metabolism, maintains the balance

in vivo through enzymatic reactions, and plays an essential role in the antioxidant defense system.[57] When exposed to oxidation conditions, GSH is converted into glutathione disulfide (GSSG),[58] making it a useful marker to probe the oxidative process of the nanocomposite dressing. The UV absorption of the GSH solution was measured after adding DTNB analysis solution (Figure 7c). The calculation showed that MgO/Ag-PCL caused a loss of GSH of over 50%, while MgO/Cu-PCL could lead to a 90% reduction, which was consistent with the corresponding visual images (Figure 7d,e). It was possibly attributed to the higher amount of ROS and released metal ions in the MgO/Cu-PCL group compared to the MgO/Ag-PCL group (Figures 4d and 5c). Both ROS and Cu^{2+} could oxidize GSH.[59,60] These results demonstrated that the nanocomposite dressings may accelerate bacterial death by disrupting the intrinsic balance.

Since Ag^+ and Cu^{2+} were released from MgO/Ag-PCL and MgO/C-PCL, respectively, in the antibacterial process, we need to confirm whether metal ions also play a bactericidal role. The antibacterial tests were performed using Ag^+ ($AgNO_3$) and Cu^{2+} ($Cu(NO_3)_2$) with the same concentrations as those released from the dressings, and no antibacterial effect was found in the presence of only metal ions (Figure S7). Therefore, it was confirmed that the bactericidal effect of the nanocomposite nanofibers was mainly caused by ROS oxidation.

3.5. Animal Wound Healing Experiment In Vivo. The cytotoxicity of the nanocomposite dressings against mouse fibroblasts in vitro was evaluated by a CCK-8 assay (Figure S8). After incubation for 24 h, the cell viability was 92% for MgO/Ag-PCL and close to 80% for MgO/Cu-PCL. The decreased viability in MgO/Cu-PCL can be attributed to the more significant released metal ions and ROS generation compared to MgO/Ag-PCL (Figures 4d and 5c), which had a negative effect on cell proliferation. However, both nanocomposite dressings maintained high cell viability, indicating that the dressings had good biocompatibility.

To evaluate the effect of the nanocomposite dressing on in vivo wound healing, an ICR mouse model with dorsal infected full-thickness skin wounds was employed, and the treatment process was established (Figure 8a). During treatment, wounds (diameter = 8 mm) infected with S. aureus (100 μL, 1×10^8 CFU/mL) were covered with either gauze or the nanofibrous dressing, and the process of wound closure was recorded. Based on the above results, we reasonably speculate that the nanocomposite dressings will inhibit S. aureus by the in situ generation of ROS and further accelerate wound healing. As expected, the nanocomposite dressings exhibited excellent antibacterial performance. As shown in Figure 8b−d, compared with the control group, the number of bacterial colonies in the PCL, MgO/Cu-PCL, and MgO/Ag-PCL groups decreased by 47.55%, 93.96%, and 90.57%, respectively, on day 2. The colony numbers of the MgO/Cu-PCL group and MgO/Ag-PCL group were significantly reduced, but there was no significant difference. These results validate the remarkable inhibitory effect of MgO-based composite dressing against S. aureus.

The wound-healing process was recorded by photographs at fixed intervals (Figure 8e). On Day 0, all wounds exhibited severe inflammatory responses with yellowish-white pus, indicating that the S. aureus-infected model was successfully established. On Day 2, the wounds in the gauze and PCL groups still suffered from much pus, while those in the MgO/

Cu-PCL and MgO/Ag-PCL groups exhibited a smaller size and decreased pus, which was consistent with the results of the in vitro antibacterial experiments. The wounds began to scab on Day 4 and showed significant healing with new skin and granulation tissue on Day 11. As shown in Figure 8f, after 2 days of treatment, the MgO/Ag-PCL group exhibited a significantly faster wound healing than other groups. The insignificant positive effect of MgO/Cu-PCL may be associated with its relatively higher cytotoxicity. After 4 days of treatment, a similar therapeutic trend was observed. Both the MgO/Ag-PCL and MgO/Cu-PCL groups significantly promoted wound healing compared to the control groups. The MgO/Ag-PCL group had the smallest relative wound area ($31.87 \pm 1.34\%$) and faster wound closure. Finally, on day 11, the wounds in the MgO/Ag-PCL and MgO/Cu-PCL groups were almost completely healed, with relative wound areas of $8.34 \pm 0.33\%$ and $9.49 \pm 1.96\%$, respectively. However, the control and PCL groups showed relative wound areas of $25.01 \pm 7.40\%$ and $15.1 \pm 1.63\%$, respectively. In general, it was indicated that the MgO/Ag-PCL and MgO/Cu-PCL composite dressings owned promising antibacterial effects and significantly promoted wound healing.

4. CONCLUSIONS

In this investigation, we successfully developed an effective antibacterial nanocomposite dressing with CDT capabilities. The dressing comprises electrospun PCL nanofibers and an electrosprayed layer containing Ag- or Cu-doped MgO NPs. These NPs are capable of producing ROS without the need for external stimulation. Notably, the electrospraying process facilitated the successful incorporation of NPs onto the surface of dressing, forming a unique string-bead structure that enabled continuous generation and release of ROS. The resulting nanocomposite dressings exhibited excellent CDT properties, ensuring their high antibacterial efficiency against both Gram-negative and Gram-positive bacteria. Accordingly, the dressings were used as wound dressings and exhibited remarkable capability in treating S. aureus-infected wounds in vivo. Overall, this innovative approach of combining electrospinning and electrospray techniques to fabricate nanocomposite nanofibers provides a promising strategy for constructing functional wound dressings with high antibacterial properties. The ROS-based antibacterial nanocomposite dressings represent a therapeutic option for addressing wound infections, offering high therapeutic value and lower susceptibility to drug resistance.

■ ASSOCIATED CONTENT

ⓢ Supporting Information

The Supporting Information is available free of charge at https://pubs.acs.org/doi/10.1021/acsomega.3c05271.

> SEM images and EDS spectra of (a, b) MgO/Ag NPs and (c, d) MgO/Cu NPs; fluorescence emission spectra of (a) MgO/Ag NPs and (b) MgO/Cu NPs with DCFH at different time points; SEM images of PCL solutions with different concentrations of (a) 0.5%, (b) 1%, (c) 2%, (d) 2.5%, and (e) 3% (w/v) by electrospraying; SEM images of the mixture of 2% (w/v) PCL and 0.4% (w/v) MgO/Ag NPs electrosprayed under different conditions. Electrospraying conditions: (a) 23 ± 2 °C, (b) 28 ± 2 °C, and (c) 33 ± 2 °C at the same humidity ($60 \pm 5\%$ RH); (d) $30 \pm 5\%$ RH, (e) $60 \pm 5\%$ RH, and

(f) 75 ± 5% RH, respectively, at the same temperature (33 ± 2 °C); fluorescence emission spectra of (a) nonporous composite microspheres and (b) monoporous composite microspheres with DCFH at different time points and (c) variation of fluorescence intensity with time; CLSM images (after reaction with DCFH) of PCL, MgO/Ag-PCL, and MgO/Cu-PCL; photographs of *E. coli* and *S. aureus* grown on agar plates after being incubated with AgNO₃ and Cu(NO₃)₂ at the same concentrations as Ag⁺ and Cu²⁺ released from nanocomposite membranes; cell viability of mouse fibroblasts 3T3 incubated with PCL, MgO/Cu-PCL, and MgO/Cu-PCL for 24 h (PDF)

■ AUTHOR INFORMATION

Corresponding Authors

Dongming Qi − *MOE Key Laboratory of Advanced Textile Materials & Manufacturing Technology, Zhejiang Sci-Tech University, Hangzhou 310018, China; Key Laboratory of Green Cleaning Technology & Detergent of Zhejiang Province, Lishui 323000, China;* orcid.org/0000-0003-3339-5339; Email: dongmingqi@zstu.edu.cn

Renhong Li − *MOE Key Laboratory of Advanced Textile Materials & Manufacturing Technology, Zhejiang Sci-Tech University, Hangzhou 310018, China;* orcid.org/0000-0002-8327-5506; Email: lirenhong@zstu.edu.cn

Jindan Wu − *MOE Key Laboratory of Advanced Textile Materials & Manufacturing Technology, Zhejiang Sci-Tech University, Hangzhou 310018, China; Key Laboratory of Green Cleaning Technology & Detergent of Zhejiang Province, Lishui 323000, China;* orcid.org/0000-0001-5255-4679; Phone: +8657186843436; Email: wujindan@zstu.edu.cn

Authors

Bingjie Xu − *MOE Key Laboratory of Advanced Textile Materials & Manufacturing Technology, Zhejiang Sci-Tech University, Hangzhou 310018, China*

Guoqiang Cai − *NICE Zhejiang Technology Co., Ltd, Hangzhou 310013, China; Key Laboratory of Green Cleaning Technology & Detergent of Zhejiang Province, Lishui 323000, China*

Yujie Gao − *MOE Key Laboratory of Advanced Textile Materials & Manufacturing Technology, Zhejiang Sci-Tech University, Hangzhou 310018, China; Key Laboratory of Green Cleaning Technology & Detergent of Zhejiang Province, Lishui 323000, China*

Mingchao Chen − *MOE Key Laboratory of Advanced Textile Materials & Manufacturing Technology, Zhejiang Sci-Tech University, Hangzhou 310018, China*

Chenlu Xu − *Department of Oral and Maxillofacial Surgery, the First Affiliated Hospital, Zhejiang University School of Medicine, Hangzhou 310003, China*

Chenglong Wang − *MOE Key Laboratory of Advanced Textile Materials & Manufacturing Technology, Zhejiang Sci-Tech University, Hangzhou 310018, China;* orcid.org/0000-0001-5211-8041

Dan Yu − *Department of Oral and Maxillofacial Surgery, the First Affiliated Hospital, Zhejiang University School of Medicine, Hangzhou 310003, China*

Complete contact information is available at:
https://pubs.acs.org/10.1021/acsomega.3c05271

Author Contributions

Bingjie Xu: investigation and writing−original draft; Guoqiang Cai: investigation and funding acquisition; Yujie Gao: investigation and writing−review and editing; Mingchao Chen and Chenlu Xu: validation; Chenglong Wang and Dan Yu: resources; Dongming Qi: supervision and funding acquisition; Renhong Li: methodology and writing−review and editing; Jindan Wu: conceptualization, funding acquisition and writing−review and editing.

Notes

The authors declare no competing financial interest.

■ ACKNOWLEDGMENTS

■ REFERENCES

(1) Homaeigohar, S.; Boccaccini, A. R. Antibacterial biohybrid nanofibers for wound dressings. *Acta Biomater.* **2020**, *107*, 25−49.

(2) Negut, I.; Grumezescu, V.; Grumezescu, A. Treatment Strategies for Infected Wounds. *Molecules* **2018**, *23* (9), 2392.

(3) Kumar, M.; Jaiswal, S.; Sodhi, K. K.; Shree, P.; Singh, D. K.; Agrawal, P. K.; Shukla, P. Antibiotics bioremediation: Perspectives on its ecotoxicity and resistance. *Environ. Int.* **2019**, *124*, 448−461.

(4) Lachiewicz, A. M.; Hauck, C. G.; Weber, D. J.; Cairns, B. A.; van Duin, D. Bacterial Infections After Burn Injuries: Impact of Multidrug Resistance. *Clin. Infect. Dis.* **2017**, *65* (12), 2130−2136.

(5) Martin, J. K.; Sheehan, J. P.; Bratton, B. P.; Moore, G. M.; Mateus, A.; Li, S. H.-J.; Kim, H.; Rabinowitz, J. D.; Typas, A.; Savitski, M. M.; et al. A Dual-Mechanism Antibiotic Kills Gram-Negative Bacteria and Avoids Drug Resistance. *Cell* **2020**, *181* (7), 1518−1532.

(6) Culp, E. J.; Waglechner, N.; Wang, W.; Fiebig-Comyn, A. A.; Hsu, Y.-P.; Koteva, K.; Sychantha, D.; Coombes, B. K.; Van Nieuwenhze, M. S.; Brun, Y. V. Evolution-guided discovery of antibiotics that inhibit peptidoglycan remodeling. *Nature* **2020**, *578* (7796), 582−587.

(7) Nadar, V. S.; Chen, J.; Dheeman, D. S.; Galván, A. E.; Yoshinaga-Sakurai, K.; Kandavelu, P.; Sankaran, B.; Kuramata, M.; Ishikawa, S.; Rosen, B. P. Arsinothricin, an arsenic-containing nonproteinogenic amino acid analog of glutamate, is a broad-spectrum antibiotic. *Commun. Biol.* **2019**, *2* (1), 1−12.

(8) Anand, U.; Carpena, M.; Kowalska-Góralska, M.; Garcia-Perez, P.; Sunita, K.; Bontempi, E.; Dey, A.; Prieto, M. A.; Proćków, J.; Simal-Gandara, J. Safer plant-based nanoparticles for combating antibiotic resistance in bacteria: A comprehensive review on its potential applications, recent advances, and future perspective. *Sci. Total Environ.* **2022**, *821*, 153472.

(9) Gordillo Altamirano, F. L.; Barr, J. J. Unlocking the next generation of phage therapy: the key is in the receptors. *Curr. Opin. Biotechnol.* **2021**, *68*, 115−123.

(10) Zhou, Q.; Si, Z.; Wang, K.; Li, K.; Hong, W.; Zhang, Y.; Li, P. Enzyme-triggered smart antimicrobial drug release systems against bacterial infections. *J. Controlled Release* **2022**, *352*, 507−526.

(11) Memar, M. Y.; Ghotaslou, R.; Samiei, M.; Adibkia, K. Antimicrobial use of reactive oxygen therapy: current insights. *Infect. Drug Resist.* **2018**, *11*, 567.

(12) Lam, P. L.; Wong, R. S. M.; Lam, K. H.; Hung, L. K.; Wong, M. M.; Yung, L. H.; Ho, Y. W.; Wong, W. Y.; Hau, D. K. P.; Gambari, R.; et al. The role of reactive oxygen species in the biological activity of antimicrobial agents: An updated mini review. *Chem.-Biol. Interact.* **2020**, *320*, 109023.

(13) Anas, A.; Sobhanan, J.; Sulfiya, K. M.; Jasmin, C.; Sreelakshmi, P. K.; Biju, V. Advances in photodynamic antimicrobial chemotherapy. *J. Photoch. Photobio. C* **2021**, *49*, 100452.

(14) Jia, Q.; Song, Q.; Li, P.; Huang, W. Rejuvenated Photodynamic Therapy for Bacterial Infections. *Adv. Healthc. Mater.* **2019**, *8* (14), 1900608.

(15) Roy, J.; Pandey, V.; Gupta, I.; Shekhar, H. Antibacterial Sonodynamic Therapy: Current Status and Future Perspectives. *ACS Biomate. Sci. Eng.* **2021**, *7* (12), 5326−5338.

(16) Jia, C.; Guo, Y.; Wu, F.-G. Chemodynamic Therapy via Fenton and Fenton-Like Nanomaterials: Strategies and Recent Advances. *Small* **2022**, *18* (6), 2103868.

(17) Pang, X.; Li, D.; Zhu, J.; Cheng, J.; Liu, G. J. N.-m. l. Beyond antibiotics: photo/sonodynamic approaches for bacterial theranostics. *Nano-Micro Lett.* **2020**, *12*, 1−23.

(18) Wang, Z.; Zhang, P.; Yin, C.; Li, Y.; Liao, Z.; Yang, C.; Liu, H.; Wang, W.; Fan, C.; Sun, D. J. A. F. M. Antibiotic-Derived Carbon-Nanodot-Decorated Hydrogel for Reactive Oxygen Species-Enhanced Anti-Infection Through Biofilm Damage. *Adv. Funct. Mater.* **2023**, *33*, 2300341.

(19) Vatansever, F.; de Melo, W. C. M. A.; Avci, P.; Vecchio, D.; Sadasivam, M.; Gupta, A.; Chandran, R.; Karimi, M.; Parizotto, N. A.; Yin, R.; et al. Antimicrobial strategies centered around reactive oxygen species − bactericidal antibiotics, photodynamic therapy, and beyond. *FEMS Microbiol. Rev.* **2013**, *37* (6), 955−989.

(20) Shan, J.; Li, X.; Yang, K.; Xiu, W.; Wen, Q.; Zhang, Y.; Yuwen, L.; Weng, L.; Teng, Z.; Wang, L. Efficient Bacteria Killing by Cu2WS4 Nanocrystals with Enzyme-like Properties and Bacteria-Binding Ability. *ACS Nano* **2019**, *13* (12), 13797−13808.

(21) Huang, S.; Xu, S.; Hu, Y.; Zhao, X.; Chang, L.; Chen, Z.; Mei, X. Preparation of NIR-responsive, ROS-generating and antibacterial black phosphorus quantum dots for promoting the MRSA-infected wound healing in diabetic rats. *Acta Biomater.* **2022**, *137*, 199−217.

(22) Demirci, S.; Yildirim, B. K.; Tünçay, M. M.; Kaya, N.; Güllüoğlu, A. N. Synthesis, characterization, thermal, and antibacterial activity studies on MgO powders. *J. Sol-Gel Sci. Techn* **2021**, *99* (3), 576−588.

(23) Aničić, N.; Vukomanović, M.; Koklič, T.; Suvorov, D. MgO Antibacterial Properties: Fewer Defects in the Surface Slows the Hydrolysis Rate, Decreases the ROS Generation Potential, and Improves the Non-ROS Antimicrobial Activity of MgO (Small 26/ 2018). *Small* **2018**, *14* (26), 1870123.

(24) Krishnamoorthy, K.; Moon, J. Y.; Hyun, H. B.; Cho, S. K.; Kim, S. J. Mechanistic investigation on the toxicity of MgO nanoparticles toward cancer cells. *J. Mater. Chemi.* **2012**, *22* (47), 24610−24617.

(25) Sawai, J.; Kojima, H.; Igarashi, H.; Hashimoto, A.; Shoji, S.; Sawaki, T.; Hakoda, A.; Kawada, E.; Kokugan, T.; Shimizu, M. J. W. J. o. M.; et al. Antibacterial characteristics of magnesium oxide powder. *World J. Microb. Biot.* **2000**, *16* (2), 187−194.

(26) Zhang, K. Q.; An, Y.; Zhang, L.; Dong, Q. Preparation of controlled nano-MgO and investigation of its bactericidal properties. *Chemosphere* **2012**, *89* (11), 1414−1418.

(27) Yang, K.; Yan, Z.; Ma, L.; Du, Y.; Peng, B.; Feng, J. A Facile One-Step Synthesis of Cuprous Oxide/Silver Nanocomposites as Efficient Electrode-Modifying Materials for Nonenzyme Hydrogen Peroxide Sensor. *Nanomaterials* **2019**, *9* (4), 523.

(28) Hussain, Z.; Thu, H. E.; Haider, M.; Khan, S.; Sohail, M.; Hussain, F.; Khan, F. M.; Farooq, M. A.; Shuid, A. N. A review of imperative concerns against clinical translation of nanomaterials: Unwanted biological interactions of nanomaterials cause serious nanotoxicity. *J. Drug Delivery Sci. Tec.* **2020**, *59*, 101867.

(29) Lan, X.; Wang, H.; Bai, J.; Miao, X.; Lin, Q.; Zheng, J.; Ding, S.; Li, X.; Tang, Y. Multidrug-loaded electrospun micro/nanofibrous membranes: fabrication strategies, release behaviors and applications in regenerative medicine. *J. Controlled Release* **2021**, *330*, 1264−1287.

(30) Dhineshbabu, N. R.; Karunakaran, G.; Suriyaprabha, R.; Manivasakan, P.; Rajendran, V. Electrospun MgO/Nylon 6 Hybrid Nanofibers for Protective Clothing. *Nano-Micro Lett.* **2014**, *6* (1), 46−54.

(31) Bedford, N. M.; Steckl, A. J. Photocatalytic Self Cleaning Textile Fibers by Coaxial Electrospinning. *ACS Appl. Mater. Interfaces* **2010**, *2* (8), 2448−2455.

(32) Chen, D.; Zhang, L.; Ning, P.; Yuan, H.; Zhang, Y.; Zhang, M.; Fu, T.; He, X. In situ growth of gold nanoparticles on electrospun flexible multilayered PVDF nanofibers for SERS sensing of molecules and bacteria. *Nano Res.* **2021**, *14* (12), 4885−4893.

(33) Sun, K.; Wang, L.; Wu, C.; Deng, J.; Pan, K. Fabrication of α-Fe2O3@rGO/PAN Nanofiber Composite Membrane for Photo-catalytic Degradation of Organic Dyes. *Adv. Mater. Interfaces* **2017**, *4* (24), 1700845.

(34) De Pieri, A.; Ocorr, K.; Jerreld, K.; Lamoca, M.; Hitzl, W.; Wuertz-Kozak, K. Resveratrol Microencapsulation into Electrosprayed Polymeric Carriers for the Treatment of Chronic, Non-Healing Wounds. *Pharmaceutics* **2022**, *14* (4), 853.

(35) Morais, A. I. S.; Vieira, E. G.; Afewerki, S.; Sousa, R. B.; Honorio, L. M. C.; Cambrussi, A.; Santos, J. A.; Bezerra, R. D. S.; Furtini, J. A. O.; Silva-Filho, E. C.; et al. Fabrication of Polymeric Microparticles by Electrospray: The Impact of Experimental Parameters. *J. Funct. Biomater.* **2020**, *11* (1), 4.

(36) Wu, J.; Ding, Y.; Wang, J.; Li, T.; Lin, H.; Wang, J.; Liu, F. *J. Mater. Chem. A* **2018**, *6* (16), 7014−7020.

(37) Ali, R.; Mehta, P.; Kyriaki Monou, P.; Arshad, M. S.; Panteris, E.; Rasekh, M.; Singh, N.; Qutachi, O.; Wilson, P.; Tzetzis, D.; et al. Electrospinning/electrospraying coatings for metal microneedles: A design of experiments (DOE) and quality by design (QbD) approach. *Eur. J. Pharm. Biopharm.* **2020**, *156*, 20−39.

(38) Li, R. H.; Zhu, X. H.; Yan, X. Q.; Kobayashi, H.; Yoshida, S.; Chen, W. X.; Du, L. L.; Qjan, K. C.; Wu, B. L.; Zou, S. H.; et al. Oxygen-Controlled Hydrogen Evolution Reaction: Molecular Oxygen Promotes Hydrogen Production from Formaldehyde Solution Using Ag/MgO Nanocatalyst. *Acs Catal.* **2017**, *7* (2), 1478−1484.

(39) Li, R.; Zhu, X.; Du, L.; Qian, K.; Wu, B.; Kawabata, S.; Kobayashi, H.; Yan, X.; Chen, W. All-solid-state magnesium oxide supported Group VIII and IB metal catalysts for selective catalytic reforming of aqueous aldehydes into hydrogen. *Int. J. Hydrogen Energy* **2017**, *42* (16), 10834−10843.

(40) Wu, J. D.; Zhao, S. F.; Xu, S. T.; Pang, X. Y.; Cai, G. Q.; Wang, J. P. Acidity-triggered charge-reversible multilayers for construction of adaptive surfaces with switchable bactericidal and bacteria-repelling functions. *J. Mater. Chem. B* **2018**, *6* (45), 7462−7470.

(41) Sun, J.; Zhang, P.; Fan, Y.; Zhao, J.; Niu, S.; Song, L.; Ma, L.; Ren, L.; Ming, W. Near-infrared triggered antibacterial nano-composite membrane containing upconversion nanoparticles. *Mater. Sci. Eng., C* **2019**, *103*, 109797.

(42) Thang, H. V.; Pacchioni, G. Oxygen Vacancy in Wurtzite ZnO and Metal-Supported ZnO/M(111) Bilayer Films (M = Cu, Ag and Au). *J. Phys. Chem. C* **2018**, *122* (36), 20880−20887.

(43) Beniya, A.; Higashi, S. Toward dense single-atom catalysts for future automotive applications. *Nature Catal.* **2019**, *2* (7), 590−602.

(44) Omidvar, A. Catalytic role of transition metals supported on niobium oxide in O2 activation. *Appl. Surf. Sci.* **2018**, *434*, 1239−1247.

(45) Zhang, D.; Lin, Y.; Song, S.; Zhang, P.; Mi, H. Study of the microstructure and antibacterial properties of MgO with doped defects. *J. Theor. Comput. Chem.* **2018**, *17* (02), 1850018.

(46) Hong, X.; Yang, Y.; Li, X.; Abitonze, M.; Diko, C. S.; Zhao, J.; Ma, Q.; Liu, W.; Zhu, Y. Enhanced anti-Escherichia coli properties of Fe-doping in MgO nanoparticles. *RSC Adv.* **2021**, *11* (5), 2892−2897.

(47) Wang, W.; Lee, G.-J.; Wang, P.; Qiao, Z.; Liu, N.; Wu, J. J. Microwave synthesis of metal-doped ZnS photocatalysts and applications on degrading 4-chlorophenol using heterogeneous photocatalytic ozonation process. *Sep. Purif. Technol.* **2020**, *237*, 116469.

(48) Wang, Z.; Du, J.; Zhang, Y.; Han, J.; Huang, S.; Hirata, A.; Chen, M. Free-standing nanoporous gold for direct plasmon enhanced electro-oxidation of alcohol molecules. *Nano Energy* **2019**, *56*, 286−293.

(49) He, T.; Jokerst, J. V. Structured micro/nano materials synthesized via electrospray: a review. *Biomate. Sci.* **2020**, *8* (20), 5555−5573.

(50) Nazir, R.; Kumar, A.; Ali Saleh Saad, M.; Ali, S. Development of CuAg/Cu2O nanoparticles on carbon nitride surface for methanol oxidation and selective conversion of carbon dioxide into formate. *J. Colloid Interface Sci.* **2020**, *578*, 726−737.

(51) Takeuchi, M.; Kurosawa, R.; Ryu, J. Vibrational spectroscopic evaluation of hydrophilic or hydrophobic properties of oxide surfaces. *J. Raman Spectrosc.* **2022**, *53*, 1793.

(52) Wang, Y.; Li, R.; Liu, Y.; Huang, Y.; Zhang, J.; Ren, X. Degradable Hemostatic Antibacterial Zein Nanofibrous Mats as Anti-Adhesive Wound Dressing. Macromol. *Mater. Engi.* **2022**, *307*, 2200241.

(53) Zhang, W. Y.; Fernandez-Fueyo, E.; Ni, Y.; van Schie, M.; Gacs, J.; Renirie, R.; Wever, R.; Mutti, F. G.; Rother, D.; Alcalde, M.; et al. Selective aerobic oxidation reactions using a combination of photocatalytic water oxidation and enzymatic oxyfunctionalizations. *Nature Catal.* **2018**, *1* (1), 55−62.

(54) Richards, T.; Harrhy, J. H.; Lewis, R. J.; Howe, A. G. R.; Suldecki, G. M.; Folli, A.; Morgan, D. J.; Davies, T. E.; Loveridge, E. J.; Crole, D. A.; et al. A residue-free approach to water disinfection using catalytic in situ generation of reactive oxygen species. *Nature Catal.* **2021**, *4* (7), 575−585.

(55) Chen, C.; Song, Z.; Zheng, X.; He, Z.; Liu, B.; Huang, X.; Kong, D.; Ding, D.; Tang, B. Z. AIEgen-based theranostic system: targeted imaging of cancer cells and adjuvant amplification of antitumor efficacy of paclitaxel. *Chemi. Sci.* **2017**, *8* (3), 2191−2198.

(56) Wang, Y.; Yang, Y.; Shi, Y.; Song, H.; Yu, C. Antibiotic-Free Antibacterial Strategies Enabled by Nanomaterials: Progress and Perspectives. *Adv. Mater.* **2020**, *32* (18), 1904106.

(57) Wang, Y.; Ledvina, H. E.; Tower, C. A.; Kambarev, S.; Liu, E.; Charity, J. C.; Kreuk, L. S. M.; Tang, Q.; Chen, Q.; Gallagher, L. A.; et al. Discovery of a glutathione utilization pathway in Francisella that shows functional divergence between environmental and pathogenic species. *Cell Host Microbe* **2023**, *31* (8), 1359−1370.

(58) Yue, J.; Mei, Q.; Wang, P.; Miao, P.; Dong, W.-F.; Li, L. A Yellow Fluorescence Probe for the Detection of Oxidized Glutathione and Biological Imaging. *ACS Appl. Mater. Interfaces* **2022**, *14* (15), 17119−17127.

(59) Huang, M.; Keller, A. A.; Wang, X. M.; Tian, L. Y.; Wu, B.; Ji, R.; Zhao, L. J. Low Concentrations of Silver Nanoparticles and Silver Ions Perturb the Antioxidant Defense System and Nitrogen Metabolism in N-2-Fixing Cyanobacteria. *Environ. Sci. Technol.* **2020**, *54* (24), 15996−16005.

(60) Fu, L. H.; Wan, Y.; Qi, C.; He, J.; Li, C.; Yang, C.; Xu, H.; Lin, J.; Huang, P. Nanocatalytic theranostics with glutathione depletion and enhanced reactive oxygen species generation for efficient cancer therapy. *Adv. Mater.* **2021**, *33* (7), 2006892.